Engineering Failure Analysis 187 (2026) 110620

Contents lists available at ScienceDirect

Engineering Failure Analysis

journal homepage: www.elsevier.com/locate/engfailanal

Wheel profile optimization for high-speed locomotives to suppress carbody hunting stability failure under complex wheel-rail conditions

Fanyu Meng, Yuan Yao *, Qun Ma, Haohao Wei

State Key Laboratory of Rail Transit Vehicle System, Southwest Jiaotong University, Chengdu 610031, China

ARTICLE INFO

Keywords:
Wheel profileoptimization
Equivalent conicity
Wheel-rail profile compatibility
Multi-objective optimization
Hunting stability failure
Surrogate model

ABSTRACT

Aiming at the problem of low-frequency carbody swaying caused by the hunting stability failure of a certain high-speed locomotive when using new reprofiling wheel in some lines at the initial stage. According to the line test, the reason is that the wheel profile has poor adaptability to the rail profile under complex conditions, resulting in a lower equivalent conicity, which leads to the carbody hunting. To solve this, the wheel profile was optimized. The nominal equivalent conicity dispersion corresponding to the matching of wheel profile with CN60 and CN60N rails under different rail cants and wheel diameter differences was taken as the optimization objective. The wheel profile is characterized by the combination of arc and straight line. The NSGA-II genetic algorithm was used to optimize the geometric parameters of the key arc to enhance the adaptability of the wheel profile to different wheel-rail conditions, and the radial basis function neural network was used to train the surrogate model to improve the optimization efficiency. Finally, the wheel-rail contact characteristics and locomotive dynamic of the wheel profile before and after optimization were compared. The results show that the optimized wheel profile significantly improves the concentration of the equivalent conicity and enhances the adaptability of the wheel profile to different line conditions. At the same time, the hunting stability, lateral ride comfort and curve passing performance index of the optimized wheel profile are improved compared with the original wheel profile. The problem of locomotives' hunting stability failure on specific lines was solved.

1. Introduction

In recent years, with the rapid development of China's railway transportation, in order to improve the ride comfort and operation speed of passengers on the existing general-speed passenger trunk lines, China has developed a variety of power centralized EMUs based on the original fast passenger electric locomotives [1]. However, with the large-scale operation of the power centralized EMUs, some dynamic problems are gradually exposed. For example, when the EMU runs to some sections, the power vehicle (high-speed locomotive) will have the problem of hunting stability failure, and the phenomenon of carbody swaying will occur, which seriously affects the ride comfort of passengers. The wheel-rail relationship has an important influence on the dynamic performance of rail vehicles, such as hunting stability, ride comfort, and running safety [2]. Hunting motion is a special phenomenon caused by the wheel-

* Corresponding author.
E-mail address: yyuan8848@163.com (Y. Yao).

https://doi.org/10.1016/j.engfailanal.2026.110620
Received 2 December 2025; Received in revised form 4 January 2026; Accepted 25 January 2026
Available online 29 January 2026

rail geometric relationship and creep force. It is a self-excited vibration caused by lateral instability. It is an inherent characteristic of the railway vehicle system and one of the core problems of vehicle system dynamics. The hunting motion of the vehicle system is divided into primary hunting (carbody hunting) and secondary hunting (bogie hunting) [3,4]. The equivalent conicity of wheel-rail contact is small or the vehicle speed is relatively low when the primary hunting occurs. At this time, the carbody vibration is large and the bogie vibration is relatively small, so it is also called carbody hunting. Secondary hunting always occurs when the vehicle is running at high speed and exceeds a certain speed critical value. The bogie hunting will maintain the periodic motion of equal amplitude and no longer decay. At this time, the carbody vibration is small and the bogie vibration is severe, so it is also called bogie hunting. Primary hunting instability will affect the running stability of the vehicle and reduce the riding comfort of passengers. Secondary hunting instability is easy to cause harmonic vibration of the bogie and cause frame alarm. In severe cases, it may even cause the wheel to collide with the rail until derailment occurs.

The optimization of wheel-rail profile is an important measure to improve the wheel-rail matching state and improve the hunting stability of the vehicle. Due to the high cost of large-scale replacement of rail profiles on existing railway lines, and the wide variety of wheel profiles of rail vehicles in China, various types of vehicles have cross-line operation, so wheel profile optimization has better economy and feasibility than rail profile optimization.

The generation methods of wheel profile include discrete point curve spline fitting method [5], wheel profile arc and straight line parameter combination method [6] and Rotary-scaling fine-tuning (RSFT) [7]. On the basis of these methods, domestic and foreign scholars have carried out a large number of wheel profile optimization studies to solve various vehicle dynamics problems. On the premise of ignoring the side roll angle of the wheelset, Shen et al. [8] based on the wheel-rail contact angle curve to invert the wheel profile and applied it to the development of independent wheelsets. Jahed et al. [9] optimized the wheel profile by using discrete points and cubic spline curves to characterize the optimization area with the goal of rolling radius difference (RRD), and verified the advantages of the new tread by dynamic software simulation. Polach [10] generated a new wheel profile by giving the target equivalent conicity, which improved the wheel-rail conformal contact and reduced the concentrated wear of the tread. Cui et al. [11] proposed a forward optimization method of wheel profile based on wheel-rail normal clearance. The new tread obtained by this method improves the distribution of contact points, reduces contact stress, and minimizes wheel-rail wear and rolling contact fatigue. Santamaria et al. [12] optimized the wheel profile according to the target equivalent conicity curve to ensure that the vehicle has good dynamic performance under different track configurations. Gan et al. [13] proposed a method to reverse the wheel profile based on the wheel diameter difference, and verified it by S1002CN and LMA profiles. Cheng et al.[14] used the arc parameters as the design variables, and carried out multi-objective optimization of the wheel profile through Isight software, which improved the low conicity carbody swaying problem of CRH3 EMU. Qi et al. [15] used the RSFT method to optimize the S1002CN profile with multiple objectives, aiming to reduce wheel wear and improve the comfort. The results were well validated through dynamic simulation. Gao et al. [16] used arc parameters to characterize the wheel profile, optimized the wheel profile of subway vehicles, reduced wheel flange wear, and improved tread rolling contact fatigue. Lin et al. [17] used discrete points to construct non-uniform rational B-spline curves to characterize wheel profiles, and used particle swarm optimization algorithm to reconstruct LM thin flange, which reduced wheel profile wear and material removal during reprofiling.

The traditional wheel profile optimization mostly considers a single wheel-rail matching condition, that is, the rail profile and the rail cant remain unchanged. However, in the actual railway line, the rail cant is discrete [18], and there will also be asymmetry of rail cant between the left and right rails. Moreover, on the domestic normal speed line, there are two profiles of CN60 rail and CN60N polished rail at the same time, so there are some limitations in considering single wheel-rail matching. Therefore, this paper not only considers the discrete situation of the rail cant, but also considers the two rail profiles of CN60 and CN60N when optimizing the wheel profile. Considering that the radius difference between the left and right wheels of the wheelset also has a great influence on the

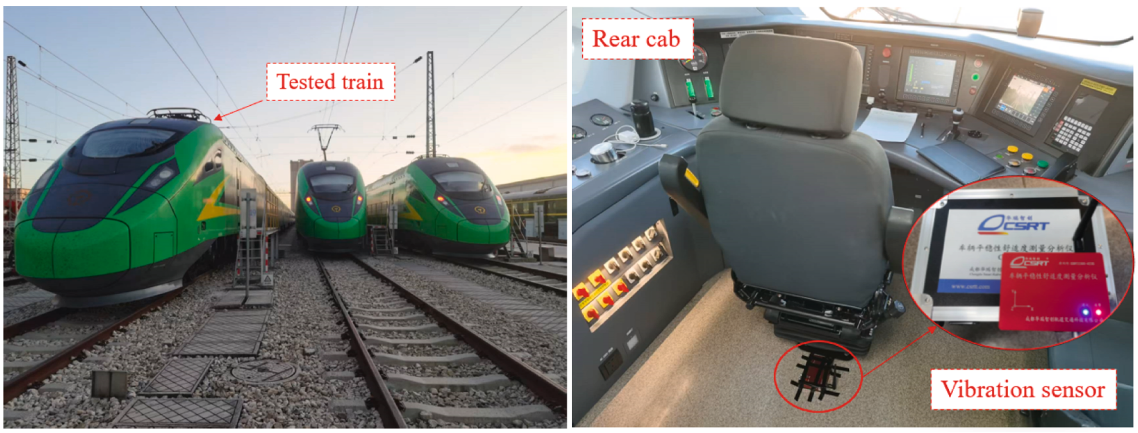

(a) Actual train (b) Sensor position

Fig. 1. Tested power-centralized EMUs.

equivalent conicity, the nominal rolling circle radius difference between the left and right wheels is also included in the optimization work. Based on the NSGA-II genetic algorithm, the two arc parameters of the rolling circle contact area of the JM_3 profile are optimized to improve its nominal equivalent conicity under different wheel-rail contact conditions, reduce the degree of dispersion, and enhance the adaptability of the wheel profile to railway lines with different wheel-rail conditions.

The layout of this paper is as follows. Section 2 analyzes the causes of hunting stability failure. Section 3 introduces the multi-objective optimization method of wheel profile. In section 4, the wheel-rail contact geometry analysis and dynamic simulation results of the wheel profile before and after optimization are compared. Section 5 summarizes and analyzes this article.

2. Failure analysis of hunting stability

Taking high-speed locomotive belongs to a certain type of CR200J power concentrated EMU as the test object, the line tracking test was carried out. The line interval is from Kunming Station to Mengzi Station in Yunnan Province, China. The test train and the installation position of vibration acceleration sensor is shown in Fig. 1. The vibration acceleration sensor was placed on the rear floor of the rear locomotive cab seat. The results of the line test are shown in Fig. 2. It can be seen that when the locomotive adopts the JM3 new wheel profile, the lateral stability index of the locomotive exceeds the standard when the EMU runs to some lines, that is, the hunting stability failure occurs, and the low-frequency lateral swaying phenomenon of about 1.12 Hz occurs. When the EMU runs for a period of time, after the wheel tread wears, the phenomenon of locomotive swaying basically disappears, and the lateral stability of the

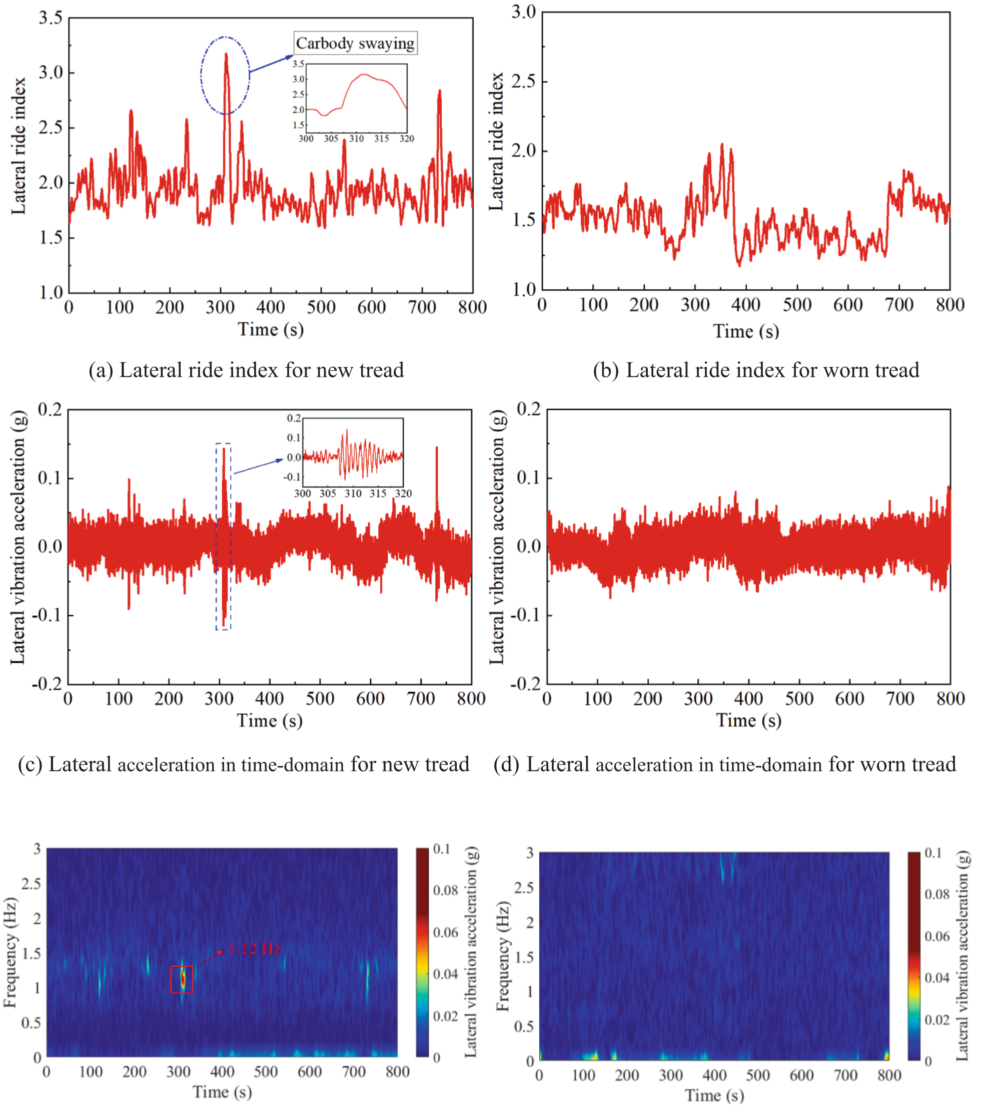

(a) Lateral ride index for new tread
(b) Lateral ride index for worn tread
(c) Lateral acceleration in time-domain for new tread
(d) Lateral acceleration in time-domain for worn tread
(e) Lateral acceleration in frequency-domain for new tread
(f) Lateral acceleration in frequency-domain for worn tread

Fig. 2. Results of line tracking test.

carbody is greatly improved.

Then, the wheel tread profile is measured, as shown in Fig. 3. The wheel tread profile of the high-speed locomotive of this type of power concentrated EMU was measured by MiniProf wheel profile measuring instrument, and the wheel profile and wheel-rail matching equivalent conicity of the new wheel and the wear wheel are compared. The wheel-rail matching condition is CN60 rail profile, and the rail cant is 1/40. It can be seen that compared with the new wheel, the wear wheel has a certain degree of wear, and the equivalent conicity of wheel-rail contact increases significantly. The nominal equivalent conicity of the new wheel at the lateral displacement of 3 mm corresponds to 0.11, and the wear wheel corresponds to 0.69. It can be seen that the equivalent conicity of wheel-rail contact has an important influence on hunting stability. At the same time, some scholars have studied the influence of equivalent conicity on the stability of hunting [19–21]. The research of Zhang et al. [22] also shows that the high-speed locomotive of this type of power concentrated EMU is easy to cause the problem of carbody hunting instability under low equivalent conicity.

Moreover, the JM_3 wheel profile is designed based on the Chinese standard 60 kg/m rail (CN60). When the wheel profile is matched with the polished rail profile (CN60N), the wheel-rail contact equivalent conicity is low because the wheel-rail contact points are concentrated on the rail top. At the same time, the equivalent conicity of the JM3 wheel profile is very sensitive to the rail cant. As shown in Fig. 4, when the rail cant is too large, the equivalent conicity of wheel-rail contact will be too low, which will easily lead to the failure of hunting stability and the phenomenon of low-frequency swaying will occur. In the actual line, the rail cant will change due to the deformation and damage of the floor plate [23]. Therefore, when the high-speed locomotive travels to some sections where the rail cant is too large, the locomotive will sway. Although optimizing the suspension parameters can slow down the low-frequency swaying phenomenon of the high-speed locomotive to a certain extent [24], the requirements of the wheel/rail vehicle's 'primary hunting' and 'secondary hunting' stability on the vehicle suspension parameters are often contradictory. In order to ensure that the power car still has good lateral stability in the wheel-rail contact state with high equivalent conicity after wheel-rail wear, the optimization and adjustment range of suspension parameters is limited [25]. Therefore, it is necessary to optimize the JM_3 wheel profile to improve its equivalent conicity and reduce the dispersion of equivalent conicity under different wheel-rail conditions. Reduce the influence of rail profile and rail cant on equivalent conicitys. Fundamentally solve the problem of high-speed locomotive hunting stability failure.

3. Multi-objective optimization method of wheel profile

3.1. Wheel profile optimization process

The multi-objective optimization method of wheel profile is mainly composed of five parts: wheel profile generation program, vehicle dynamics model, wheel-rail contact stress finite element calculation model, surrogate model and optimization algorithm. The specific optimization process is shown in Fig. 5, and the process is as follows:

(1) Based on MATLAB, the wheel profile generation program with design variables as input is written.

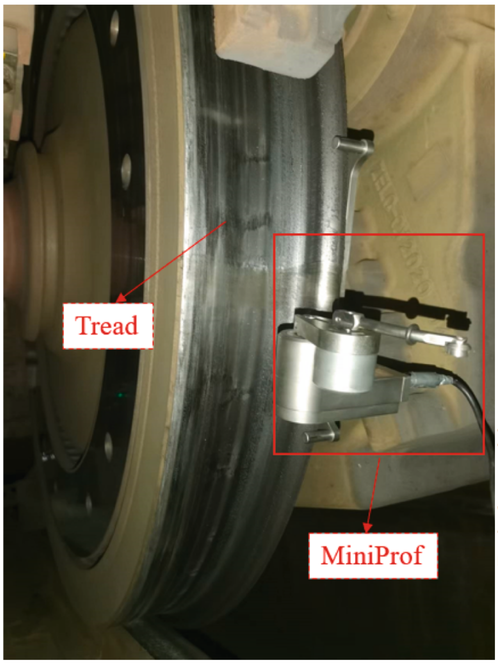

(a) Measuring instruments and objects

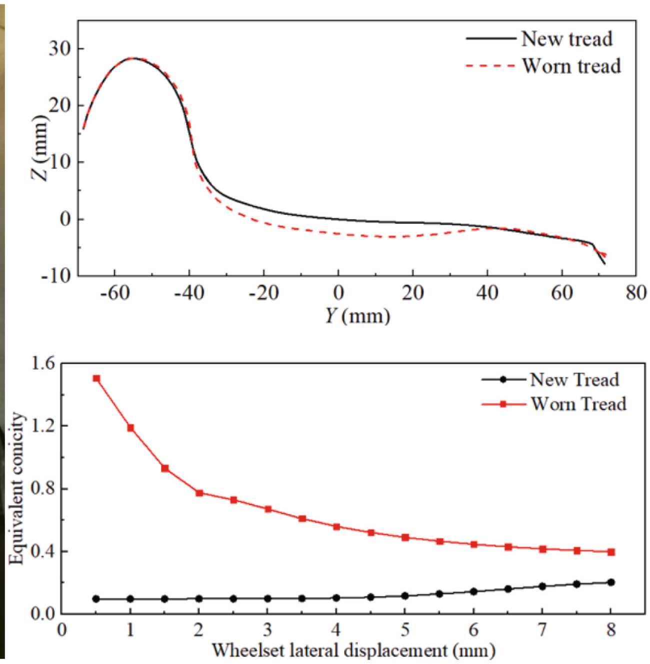

(b) Comparison of measured wheel profiles

Fig. 3. Measurement of wheel tread profile.

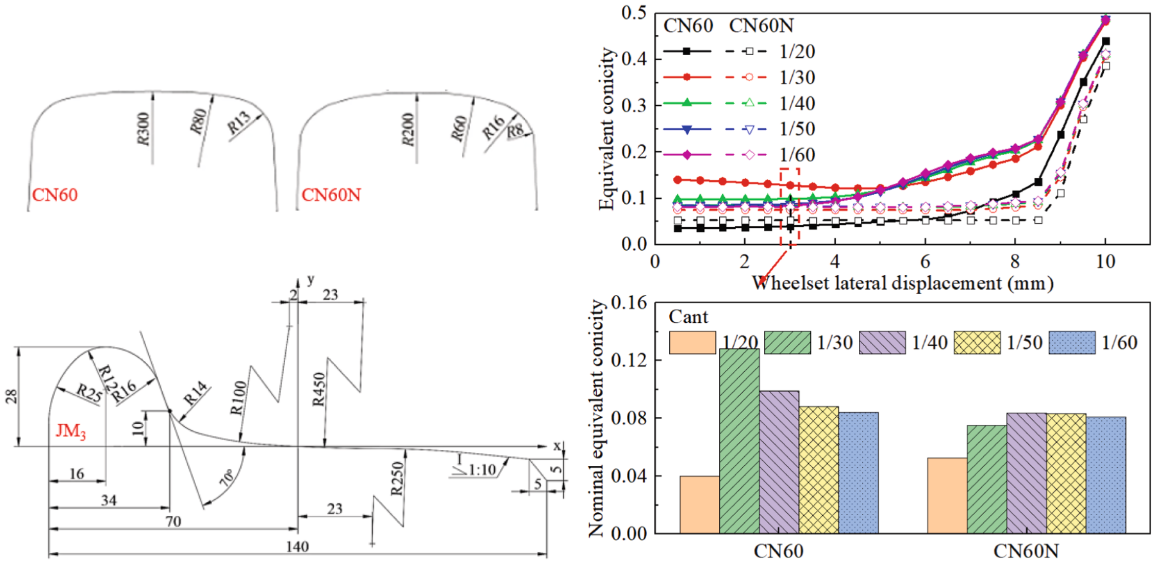

(a) Standard rails and wheel profiles (b) Wheel-rail matching equivalent conicity

Fig. 4. Wheel/rail profiles and matching characteristics.

(2) The vehicle dynamics model is established based on SIMPACK.

(3) The finite element calculation model of wheel-rail contact stress is established based on ABAQUS.

(4) Construct a surrogate model that reflects the mapping relationship between design variables and objective functions and constraint functions. Latin hypercube sampling is performed on the design variables within the value range to obtain a certain number of sample parameters. A wheel profile generation program is used to obtain wheel profiles corresponding to the sample parameters.

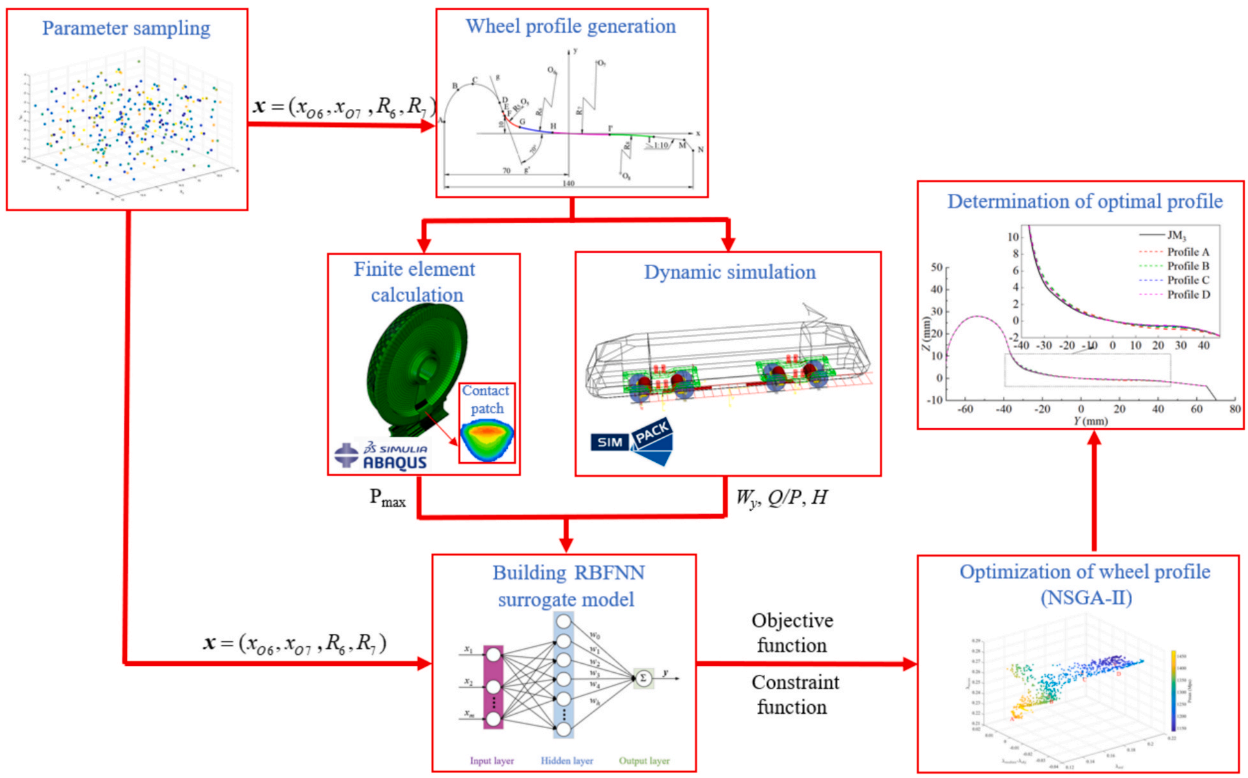

Fig. 5. Multi-objective optimization process of wheel profile.

The wheel profile is introduced into the vehicle dynamics model and the wheel-rail contact stress finite element calculation model to carry out dynamics simulation and wheel-rail contact stress calculation, and the correlation calculation value of the objective function value and the constraint function is obtained. The objective function selects the calculated wheel-rail contact stress, and the constraint function selects the dynamic indexes related to vehicle ride comfort and running safety. The surrogate model is constructed by using the sample parameters, objective function values and constraint function correlation values and its accuracy is verified.

(5) The surrogate model is applied to the multi-objective optimization algorithm to optimize the wheel profile. The optimized parameters are input into the wheel profile generation program to obtain the optimized profile, and then imported into the vehicle dynamics model for simulation to verify.

3.2. Wheel profile description method

Because the discrete point curve spline fitting method describes the wheel profile, too many optimization variables, and also need to consider the monotony and convexity of the wheel profile curve, resulting in low computational efficiency. Although the RSFT method has few optimization parameters, the height, width and angle of the flange of the new wheel profile will change. However, the method of describing wheel profile by combining arc and straight line characteristic parameters of wheel profile can ensure less optimization variables, and at the same time, due to geometric constraints, it can well ensure the smoothness and convexity of each curve connection, which can greatly improve the calculation efficiency [26]. At the same time, the common wheel profile is shown in Fig. 6, which is composed of multiple segments and arcs, so this paper uses the combination method of arcs and segments to describe the wheel profile. EI segment is selected as optimization area, which consists of 4 arcs. The arcs are $\widehat{EG}$, $\widehat{GH}$, $\widehat{HI'}$ and $\widehat{I'I}$. Let the center of the four arcs and their coordinates are $O_5(x_{O5}, y_{O5})$, $O_6(x_{O6}, y_{O6})$, $O_7(x_{O7}, y_{O7})$, $O_8(x_{O8}, y_{O8})$, and the radii are R_5, R_6, R_7, R_8, respectively. By using arc parameters to characterize the wheel profile through geometric constraints, the 12 arc parameters (center transverse and vertical coordinates and radius) describing the four arcs of EI segment can be reduced to 6 parameters, which are R_5, R_6, x_{O6}, R_7, x_{O7}, and R_8. The following equations (1) to (4) [27] are obtained according to the constraint conditions:

From the arc $\widehat{HI'}$ passing through the base point O (0, 0), we can get

$$y_{O7} = \sqrt{R_7^2 - x_{O7}^2} \tag{1}$$

It can be obtained by inscribing arc $\widehat{GH}$ and arc $\widehat{HI'}$

$$y_{O6} = y_{O7} - \sqrt{(R_7 - R_6)^2 - (x_{O7} - x_{O6})^2} \tag{2}$$

From the fact that the arc $\widehat{EG}$ is tangent to both the straight line gg' and the arc $\widehat{GH}$, the simultaneous equations can be obtained:

$$\begin{cases} x_{O5} = \left(-b_1 + \sqrt{b_1^2 - 4a_1c_1}\right)/2a_1 \\ y_{O5} = y_{O6} - \sqrt{(R_5 - R_6)^2 - (x_{O5} - x_{O6})^2} \end{cases} \tag{3}$$

In Eq. (3),

$$a_1 = 1 + k_{gg'}^2$$

$$\delta_1 = b_{gg'} + R_5\sqrt{1 + k_{gg'}^2} - y_{O6}$$

$$b_1 = 2\left(k_{gg'}\delta_1 - x_{R6}\right)$$

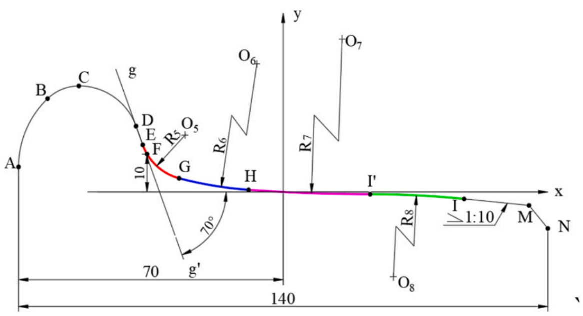

Fig. 6. Circular arc wheel profile diagram.

$$c_1 = x_{O6}^2 + \delta_1^2 - (R_5 - R_6)^2$$

$$k_{gg'} = -\tan 70^\circ$$

$$b_{gg'} = y_D - k_{gg'} x_D$$

where x_D and y_D are the horizontal and vertical coordinates of point D.

From the fact that the arc $\widehat{I'I}$ is tangent to both the straight line IM and the arc $\widehat{HI'}$, the simultaneous equations can be obtained:

$$\begin{cases} x_{O8} = \left(-b_2 + \sqrt{b_2^2 - 4a_2c_2}\right)/2a_2 \\ y_{O8} = y_{O7} - \sqrt{(R_8 - R_7)^2 - (x_{O8} - x_{O7})^2} \end{cases} \tag{4}$$

In equations (4),

$$a_2 = 1 + k_{IM}^2$$

$$\delta_2 = b_{IM} - R_8\sqrt{1 + k_{IM}^2} - y_{O7}$$

$$b_2 = 2(k_{IM}\delta_2 - x_{O7})$$

$$c_2 = x_{O7}^2 + \delta_2^2 - (R_7 + R_8)^2$$

$$k_{IM} = -0.1$$

$$b_{IM} = y_M - k_{IM} x_M$$

where x_M and y_M are the horizontal and vertical coordinates of point M.

3.3. Multi-objective optimization mathematical model

The mathematical model of wheel profile multi-objective optimization adopted in this paper is:

$$\min_{x_{kl} \le x_k \le x_{ku}} : \{f_i(\boldsymbol{x})\} i = 1, 2, 3, 4 \tag{5}$$

$$\boldsymbol{s.t.} : g_j(\boldsymbol{x}) \le 0 j = 1, 2, 3 \tag{6}$$

where x_{ku} and x_{kl} are the upper and lower bounds of the design variable x_k, $k = 1, 2, 3, 4$. $f_i(\boldsymbol{x})$ is the objective function, $g_j(\boldsymbol{x})$ is the constraint function.

3.3.1. Design variables

According to Section 3.2, in order to further reduce the number of optimization variables, this paper optimizes the two arcs of the constant contact area, which are $\widehat{GH}$ and $\widehat{HI'}$. In order to match the flange root arc curve better with the rail shoulder radius of CN60 and CN60N, R_5 is taken as 15 mm, while R_8 remains unchanged and is taken as 250 mm. Therefore, R_6, x_{O6}, R_7 and x_{O7} are selected as design variables, that is, $\boldsymbol{x}=(x_1, x_2, x_3, x_4) = (R_6, x_{O6}, R_7, x_{O7})$. Referring to the size of various wheel profiles in the standard TB/T 449-2016 [28], the upper and lower limits of the design variables are given, and the upper and lower limits of the variables are set in Table 1.

3.3.2. Objective functions

In order to improve the wheel-rail matching equivalent conicity of JM3 profile, and reduce the sensitivity of wheel-rail matching equivalent conicity to rail profile, rail cant and initial wheel diameter difference. CN60 and CN60N rail profiles are selected for calculation of nominal equivalent conicity; denominator values of left and right rail cants are both in the range of 20 ∼ 60, with an

Table 1
Upper and lower limits of design variables.

Design variables	Lower (mm)	Upper (mm)
R_6	90.0	120.0
x_{O6}	−4.0	−1.0
R_7	380.0	500.0
x_{O7}	22.0	27.0

interval of 5; initial wheel diameter difference values ΔR are in the range of 0~2 mm, with an interval of 1 mm. The above conditions are arranged and combined to form a total of 486 wheel-rail matching conditions.

(1) In order to reflect the concentration of the nominal equivalent conicity, the standard deviation of the nominal equivalent conicity of the wheel profile matched with the two rails with different rail cants conditions is taken as the objective function $f_1(\boldsymbol{x})$:

$$f_1(\boldsymbol{x}) = \lambda_{std} \tag{7}$$

(2) In order to make the nominal equivalent conicity of the normal wheel profile concentrate around 0.1, the difference between the median and 0.1 of the nominal equivalent conicity matched with the rail under the above conditions when the wheel diameter difference is 0 mm is taken as the objective function $f_2(\boldsymbol{x})$:

$$f_2(\boldsymbol{x}) = \lambda_{median} - \lambda_{obj} \tag{8}$$

(3) In order to ensure that the equivalent conicity is not too large when there is a wheel diameter difference between the left and right wheels, the average value of the nominal equivalent conicity calculated by the above 486 wheel-rail matching conditions is taken as the objective function $f_3(\boldsymbol{x})$:

$$f_3(\boldsymbol{x}) = \lambda_{mean} \tag{9}$$

(4) In order to ensure that the wheel-rail contact stress is not too large, the maximum stress of the wheelset in contact with CN60 and CN60N at 0 and 3 mm is selected as the objective function $f_4(\boldsymbol{x})$:

$$f_4(\boldsymbol{x}) = \max\{P_{60\_0mm}, P_{60\_3mm}, P_{60N\_0mm}, P_{60N\_3mm}\} \tag{10}$$

3.3.3. Constraint functions

(1) The constraint function $g_1(\boldsymbol{x})$ for lateral ride comfort is:

$$g_1(\boldsymbol{x}) = \max\{(W_y)_n\} - (W_y)_0 \tag{10}$$

where W_y is the lateral ride index of the locomotive, $(W_y)_0$ is the limit value of excellence for evaluating the ride index given by the standard GB/T 5599-2019 [29], and $(W_y)_0 = 2.75$.

(2) The constraint function $g_2(\boldsymbol{x})$ related to the derailment coefficient is:

$$g_2(\boldsymbol{x}) = \max\{(Q/P)_n\} - (Q/P)_0 \tag{11}$$

where Q is the lateral force of the wheel, P is the vertical force of the wheel, $(Q/P)_0$ is the limit value of the derailment coefficient limit given by the standard, and $(Q/P)_0 = 0.8$.

(3) The constraint function $g_3(\boldsymbol{x})$ related to the wheelset lateral force is:

$$g_3(\boldsymbol{x}) = \max\{H_n\} - H_0 \tag{12}$$

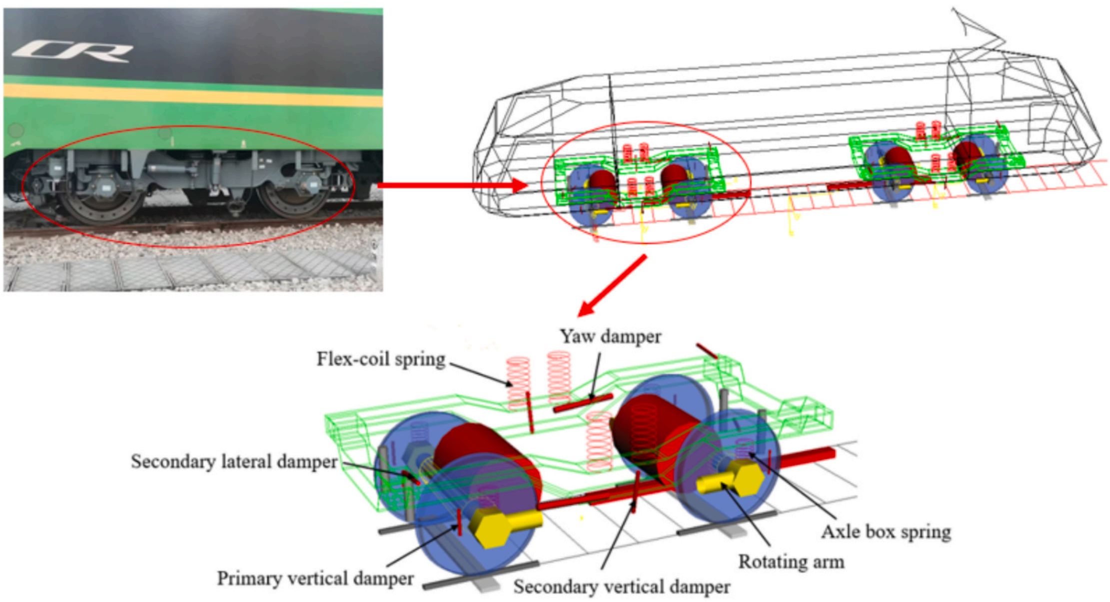

Fig. 7. Dynamic model of high-speed locomotive.

where H is the wheelset lateral force, H_0 is the wheelset lateral force limit calculated according to the standard, $H_0 = 77$ kN.

3.4. Vehicle dynamics model

The multi-body dynamics commercial software SIMPACK is used to establish the dynamic model of high-speed locomotive of the power concentrated EMU. As shown in Fig. 7, the vehicle model consists of 25 rigid bodies, including 4 wheelsets, 8 axle boxes, 2 frames, 4 hollow shafts, 4 motors, 2 traction rods and 1 carbody. with a total of 90 degrees of freedom. Among them, the wheel-rail considers the nonlinear contact relationship, and the wheel-rail tangential force adopts the FASTSIM algorithm [30].

The suspension system of the high-speed locomotive is composed of a primary suspension and a secondary suspension. The primary suspension acts between the wheels and the frame, including the axle box rotating arm, the axle box spring and the primary vertical damper. The secondary suspension acts between the frame and the car body, including the secondary flex-coil spring, secondary lateral damper, secondary vertical damper, anti-yaw damper and lateral stop. Both the dampers and the stop take into account the nonlinear characteristics. Some parameters of the vehicle are shown in Table 2. The accuracy of the vehicle dynamics model has been verified in previous papers [31,32], so it is not repeated here.

3.5. Finite element calculation model of wheel-rail contact stress

The finite element analysis software ABAQUS is used to establish the finite element calculation model of wheel-rail contact stress, and the wheel-rail contact stress at the position of 0 mm and 3 mm when the wheel profile is matched with CN60 and CN60N rails is calculated respectively. The finite element model is shown in Fig. 8.

3.6. Surrogate model

In the optimization process, in order to make the wheel profile meet the constraint function and select the optimal variables in the objective function, it is necessary to calculate the dynamic performance of a large number of wheel profiles. If only SIMPACK software is used for simulation, it will take a lot of time and seriously affect the computational efficiency. The introduction of the surrogate model can reduce the calculation time and improve the calculation efficiency while ensuring the accuracy of the calculation results. Common surrogate models include polynomial response surface model, Kriging model and neural network model. Among them, the radial basis function neural network (RBFNN) surrogate model is simple to train, has a fast learning speed while maintaining good approximation ability, and is widely used in practical engineering fields. The structure of RBFNN surrogate model [33] is shown in Fig. 9. This model consists of three layers of forward network, which are input layer, hidden layer and output layer. Its working principle is that the input layer inputs m input parameters into the model in the form of vector $\boldsymbol{x} = [x_1, x_2, \ldots, x_m]^T$, and performs nonlinear transformation by the radial basis function neurons in the hidden layer. Finally, the output layer performs linear transformation, and outputs a vector $\boldsymbol{y} = [y_1, y_2, \ldots, y_n]^T$ composed of n responses.

Theoretically, RBFNN has the ability to approximate any complex nonlinear mapping, which can be expressed as:

$$f = \boldsymbol{R}^m \rightarrow \boldsymbol{R}^n \tag{14}$$

According to the definition, the calculation formula of the output response is:

$$\boldsymbol{y} = f(\boldsymbol{x}) = w_0 + \sum_{i=1}^{h} w_i \phi(\|\boldsymbol{x} - \boldsymbol{u}_i\|) \tag{15}$$

In the equation, $\boldsymbol{x} \in \boldsymbol{R}^m, \boldsymbol{y} \in \boldsymbol{R}^n$, h represents the number of neurons in the hidden layer, $\boldsymbol{u}_i$ is the center vector of the hidden nodes in the hidden layer, $\boldsymbol{u}_i \in \boldsymbol{R}^m$, w_0 represents the deviation value, w_i represents the weighting coefficient, $||\bullet||$ represents the Euclidian norm, and $\phi(\bullet)$ represents the Gaussian radial basis function.

In order to ensure the accuracy of the surrogate model, the deterministic coefficient R^2 is introduced to evaluate the accuracy of the model [34]. The calculation formula is as follows:

Table 2
Main parameters of the powered vehicle.

Item	Value	Unit
Axle load	19.5	t
Carbody mass	42.907	t
Bogie frame mass	3.442	t
Wheelset mass	2.434	t
Bogie wheelbase	2.9	m
Distance between bogie centres	9	m
Distance of contact point	1.493	m
Wheel rolling circle diameter	0.625	m
Wheel profile type	JM3	–

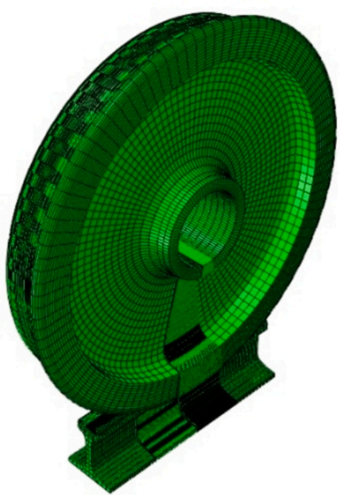

Fig. 8. Finite element model of wheel-rail contact.

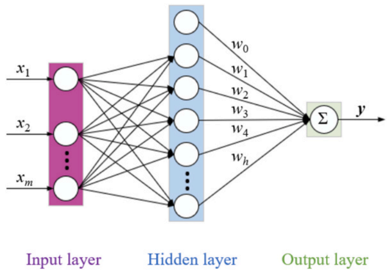

Fig. 9. The principle diagram of radial basis function neural network surrogate model.

$$R^2 = 1 - \sum_{i=1}^{n} (y_i - \widehat{y}_i)^2 / \sum_{i=1}^{n} (y_i - \overline{y}_i)^2 \tag{16}$$

In the equation, n represents the number of test samples, y_i represents the test value of the test sample, $\widehat{y}_i$ represents the calculation result of the surrogate model, and $\overline{y}_i$ represents the average value of the test value in the test sample. The R^2 value is between 0 and 1, and the closer the R^2 value is to 1, the more accurate the surrogate model is.

In this paper, the optimal Latin hypercube sampling method is used to sample the design variables to ensure the uniformity of the

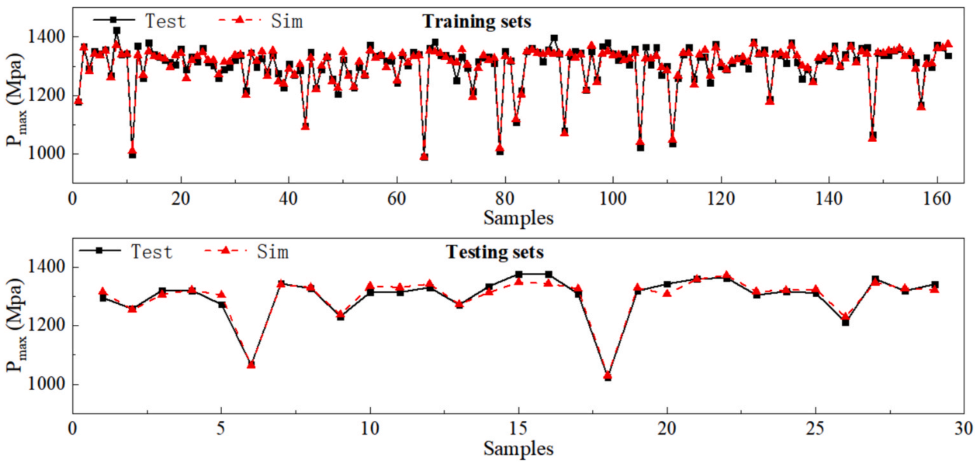

Fig. 10. The training results of the surrogate model.

spatial distribution of the sample points. In the range of design variables, about 200 sets of wheel profile samples are generated and imported into the vehicle dynamics model for simulation calculation. 85% of the data are randomly selected for training the surrogate model, and the remaining 15% of the data are used for model verification. The experience shows that when the deterministic coefficient R^2 is greater than 0.8, the surrogate model can predict the value that meets the accuracy of the optimization design requirements [35]. The deterministic coefficient R^2 of the surrogate model constructed in this paper is greater than 0.9, indicating that the model has good fitting ability and high accuracy. Meet the requirements of optimization design. The training results of the wheel-rail maximum contact stress surrogate model are shown in Fig. 10.

3.7. Optimistic algorithm

Because the NSGA-II genetic algorithm can accelerate the convergence speed of the algorithm and improve the computational efficiency while retaining the elite solution set of different emphases, the algorithm is used to optimize the four objective functions at the same time, and the obtained Pareto optimization frontier is shown in Fig. 11. The K-means clustering method [36] is used to classify the frontiers. The number of cluster centers is set to 4, and the parameters corresponding to the 4 centers are rounded, as shown in Table 3. The generated four wheel profiles and the original JM3 profile are shown in Fig. 12(a). Fig. 12(b)-(d) shows the distribution of nominal equivalent conicity of five wheel profiles under different wheel diameter differences. It can be seen from the figure that the nominal equivalent conicity of the A profile is relatively concentrated compared with other profiles. At the same time, when the wheel diameter difference is 0 mm, there is no too small nominal equivalent conicity. Therefore, the A profile has better line adaptability, so the A profile is selected as the optimal surface, named Opt A.

4. Analysis of optimization results

To comprehensively evaluate the performance of the optimized profile, this study involved wheel-rail contact geometry analysis and dynamic simulations for both the original JM_3 and optimized profiles. The validation was conducted with the following sequence: first testing the critical speed and stability, and then sequentially assessing ride comfort, curving performance, and wear performance.

4.1. Wheel-rail contact geometry analysis

Fig. 13 shows the wheel-rail contact point distribution corresponding to the matching of the original standard JM_3 profile and the optimized wheel profile Opt A with the CN60 and CN60N rails under the condition of 1/20 of the large rail cant. By comparison, under different matching conditions, the distribution of wheel-rail contact points on the optimized wheel profile is wider and more uniform than that on the JM_3 profile, which avoids the problem that the contact points are too concentrated in the rail top area. When the rail cant is 1/40, the distribution of wheel-rail contact points before and after optimization is not much different, so there is no display here.

Fig. 14 is the comparison of the equivalent conicity curve and the nominal equivalent conicity value before and after the

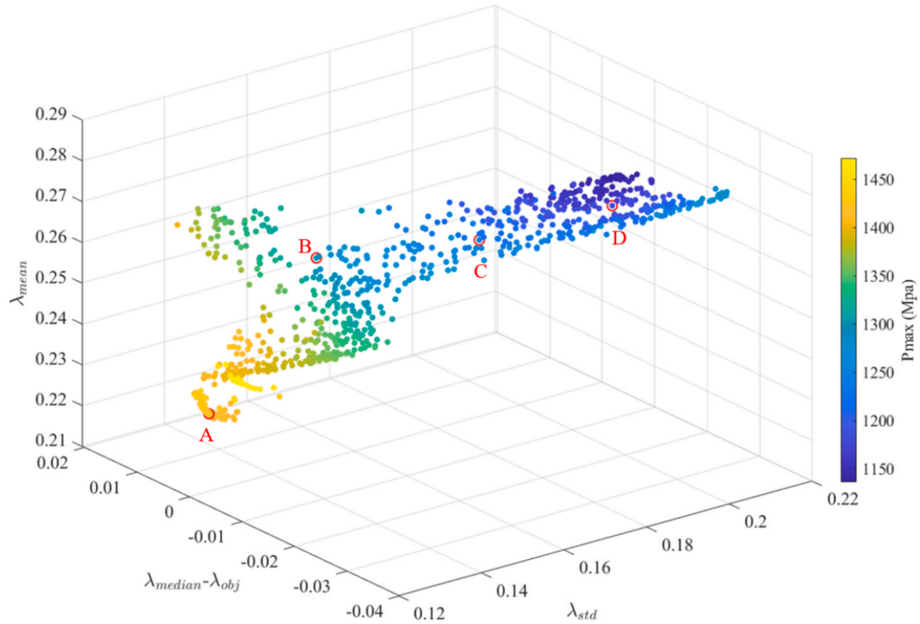

Fig. 11. Pareto front.

Table 3
The profile parameters corresponding to the four clustering centers.

Profile	R_6 (mm)	x_{O6} (mm)	R_7 (mm)	$x_{O7\text{(mm)}}$
A	100	−1	380	27
B	90	−1	460	26
C	95	−1	465	23.5
D	95	−1	490	22.5

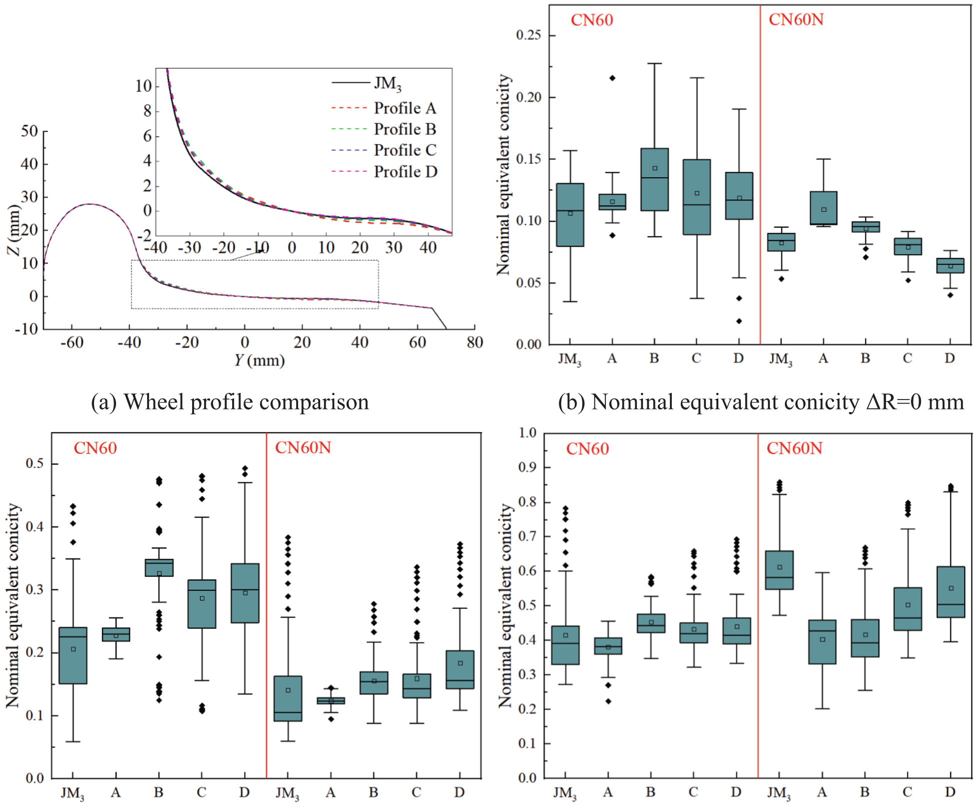

(a) Wheel profile comparison (b) Nominal equivalent conicity ΔR=0 mm

(c) Nominal equivalent conicity ΔR=1 mm (d) Nominal equivalent conicity ΔR=2 mm

Fig. 12. Comparison of wheel profile before and after optimization.

optimization of the wheel profile. By comparison, it can be seen that the equivalent conicity of the optimized wheel profile is larger than that of the JM_3 profile, and the sensitivity to rail profile and rail bottom slope is reduced. Compared with the JM_3 profile, the optimized wheel profile does not have the problem of too low equivalent conicity under different matching conditions, and also reduces the dispersion of equivalent conicity.

4.2. Stability analysis

Stability is determined using the deceleration method [37] to solve for the nonlinear critical speed. Given the initial speed of the high-speed locomotive, initial disturbance is applied to the wheelset to cause instability, while a constant external force is applied to the locomotive to cause uniform deceleration. The convergence of the lateral displacement of the wheelset during operation is examined to determine the stability of the power vehicle. Fig. 15 shows the nonlinear critical speeds corresponding to different matching conditions before and after wheel profile optimization. It can be seen that the optimized wheel profile Opt A exhibits a significant improvement in nonlinear critical speed compared to the original standard JM_3 wheel profile, particularly under the 1/20 rail cant condition, where the nonlinear critical speed is greatly enhanced, meeting the requirements for high-speed operation. Specifically, under the rail cant of 1/40, when matched with CN60 rails, the nonlinear critical speed increases from 395 km/h to 450 km/h, representing a 13.9% improvement; when matched with CN60N rails, the nonlinear critical speed increases from 660 km/h to 740 km/h, representing a 12.1% improvement; Under the rail cant of 1/20, when paired with CN60 rails, the nonlinear critical speed increased from 200 km/h to 395 km/h, representing a 97.5% increase; when paired with CN60N rails, the nonlinear critical speed

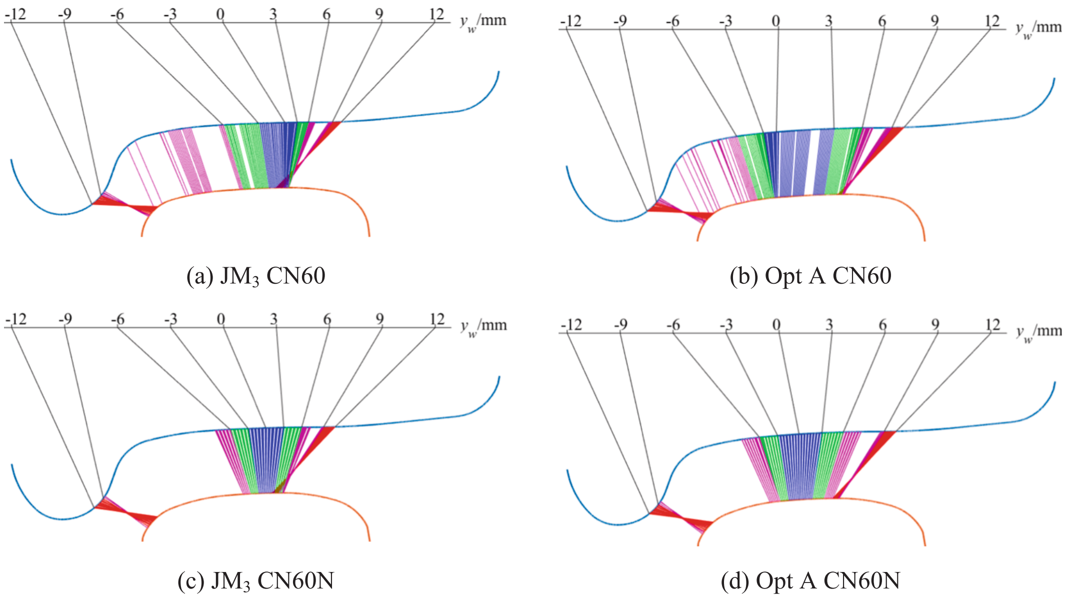

Fig. 13. Distribution of wheel-rail contact points under different matching condition.

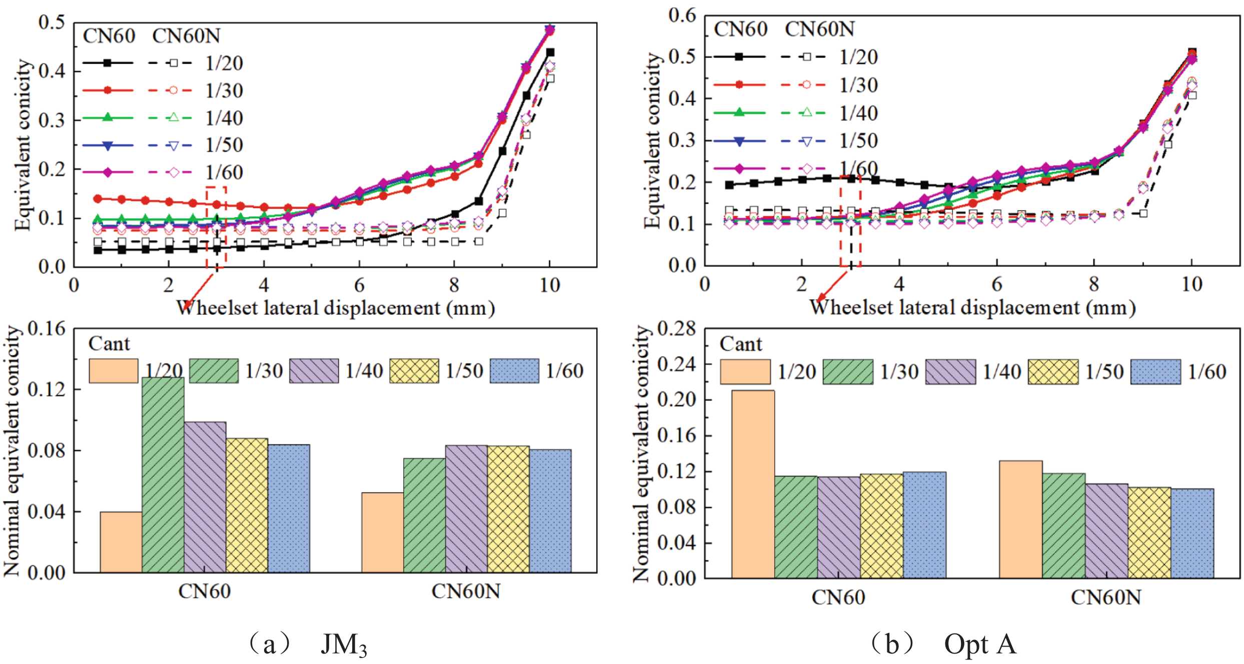

Fig. 14. Comparison of equivalent conicity before and after wheel profile optimization.

increased from 200 km/h to 600 km/h, representing a 200% increase.

4.3. Ride comfort analysis

The vehicle ride comfort calculation uses the actual track spectrum measured on the Wuhan-Guangzhou line as the track excitation, with the speed range set at 80–240 km/h. The comparison of the lateral ride index before and after wheel profile optimization is shown in Fig. 16(a) and (b). Within this speed range, the lateral ride index corresponding to the optimized wheel profile Opt A are all within 2.75, meeting the standard for excellent locomotive running stability. However, the original standard JM3 profile exhibits degraded lateral ride index under certain wheel-rail matching conditions during high-speed operation, with lateral ride index exceeding 2.75,

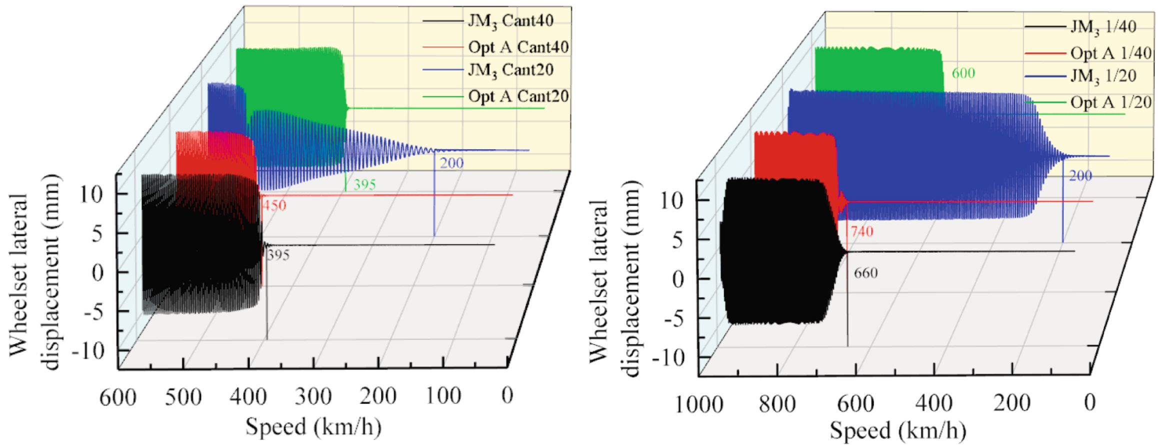

（a） CN60 （b） CN60N

Fig. 15. Comparison of nonlinear critical speed before and after wheel profile optimization.

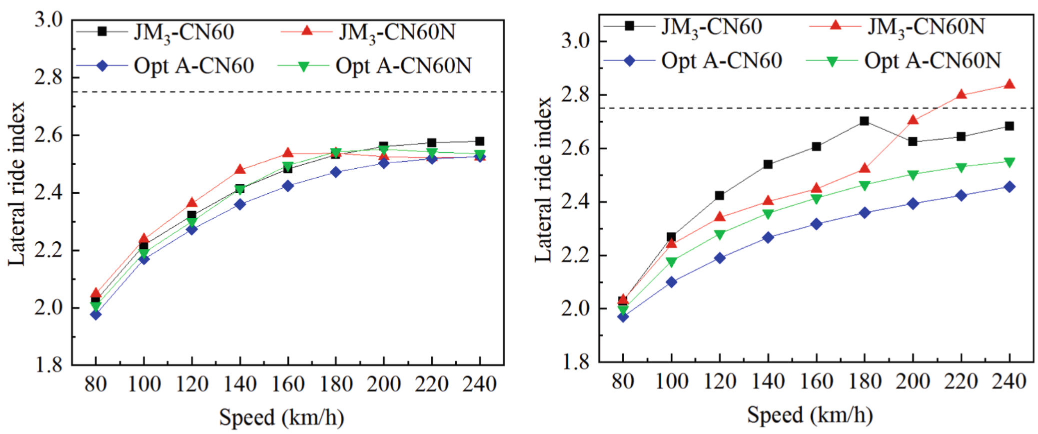

(a) Rail cant: 1/40 (b) Rail cant: 1/20

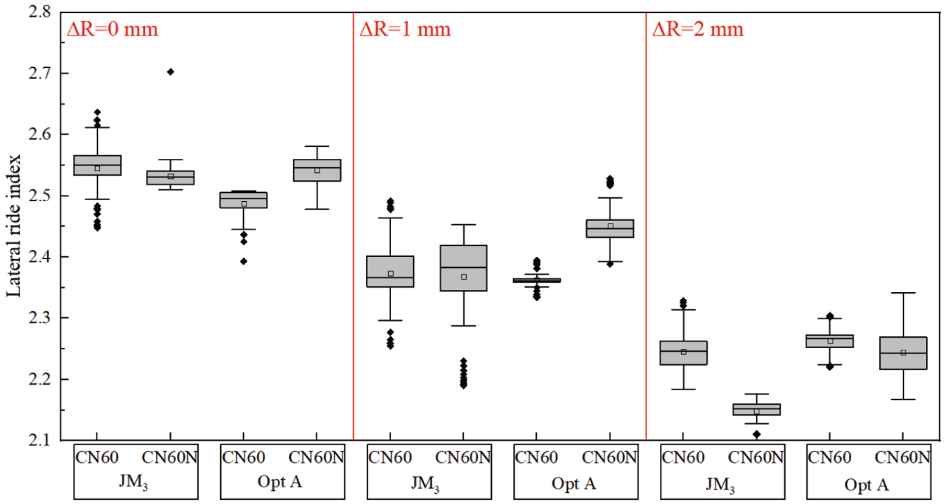

(c) The distribution of lateral ride index under different wheel-rail matching conditions

Fig. 16. Comparison of lateral ride index before and after wheel profile optimization.

resulting in low-frequency swaying phenomena, and thus failing to meet the superior-grade standards for locomotive lateral ride comfort. As shown in Fig. 16(a), under the rail cant of 1/40, the lateral ride index of the Opt A wheel profile is very close to that of the original JM3 wheel profile, with a maximum decrease of 2.4%; As shown in Fig. 16(b), when the rail cant is 1/20, compared to the original JM3 wheel profile, the lateral ride index corresponding to the optimized wheel profile Opt A shows a very small change trend with increasing speed, and there is no issue of lateral stability deterioration during high-speed operation of the locomotive. When matched with CN60 and CN60N rails, the lateral ride index decreased by a maximum of 12.7% and 10.1%, respectively. Additionally, the lateral ride index of the optimized wheel profile under the aforementioned four matching conditions are very similar, enhancing the wheel profile's adaptability to different rail profiles and rail cants.

Taking a running speed of 200 km/h as an example, this study investigates the distribution of lateral ride comfort of the carbody before and after wheel profile optimization under different wheel-rail matching conditions, as shown in Fig. 16(c). It can be seen that the optimized profile Opt A has relatively concentrated lateral ride comfort compared to the original JM3 profile, especially when the wheel diameter difference is 0 mm, and there is no situation where the ride index is too large.

4.4. Curve performance analysis

The curve-passing performance index corresponding to the wheel profile before and after optimization are shown in Fig. 17. The curve-passing performance index corresponding to the wheel profile before and after optimization are both below the safety limit. Among them, the curve-passing performance index corresponding to the Opt A wheel profile are very similar to those of the JM3 wheel profile under small-radius curve conditions. As the curve radius increases, the improvement effect also increases. Among these, the wheelset lateral force and the derailment coefficient show significant improvement compared to the wheel unloading rate. Under R1600 curve conditions, compared to the JM3 wheel profile, the Opt A wheel profile, when matched with CN60 and CN60N rails under the rail cant of 1/40, reduces wheelset lateral force by 5.2% and 22.3%, respectively, while the derailment coefficient remains unchanged when matched with CN60 rails and decreases by 22.6% when matched with CN60N rails; Under the rail cant of 1/20, when matched with CN60 and CN60N rails, the wheelset lateral force decreased by 33.5% and 35.7%, respectively, and the derailment coefficient decreased by 37.5% and 32.4%, respectively.

4.5. Wear performance analysis

Wear number is an important index used to judge the wheel wear [38], which is close to the actual wear of the wheel. The calculation formula is as follows:

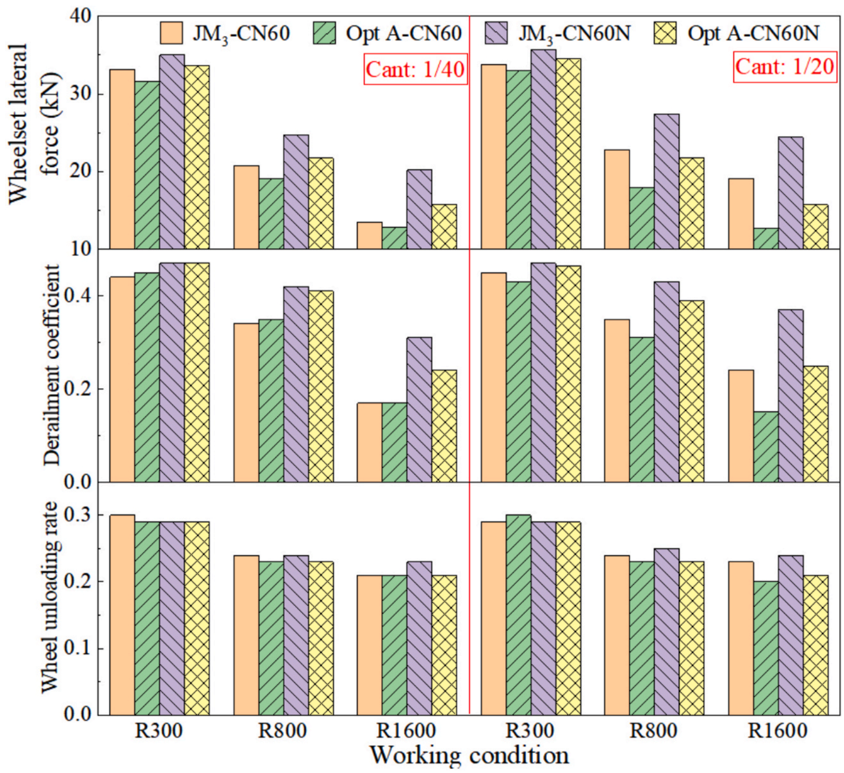

Fig. 17. Comparison of curve passing performance indexes.

$$W = T_x\gamma_x + T_y\gamma_y \tag{17}$$

In the equation, T_x and T_y are longitudinal and lateral creep forces, respectively; γ_x and γ_y are longitudinal and lateral creepage rates, respectively.

Taking the R300 small radius curve as an example, the comparison of the wear number of the wheel profile before and after optimization is shown in Fig. 18. The corresponding wear number of the wheel profile before and after optimization is roughly the same, indicating that the wear performance is basically the same.

In addition to improving dynamic performance, the optimized wheel profile should also possess excellent wear resistance. To further verify the favorable wear performance of the optimized wheel, a wheel wear prediction model was established based on the USFD wear model [39], and wear simulation was conducted for both the original and optimized wheel profiles. During the simulation, the wheel profile was updated each time the wear depth reached 0.1 mm. Wheel profiles with similar service mileage were then selected for comparative analysis of wear evolution and dynamic performance.

Fig. 19 illustrates the wheel wear conditions and dynamic performance comparisons under different operating mileages. As shown in Fig. 19(c), with the increase in service mileage, the nonlinear critical speed corresponding to the Opt A profile remains consistently higher than that of the JM_3 profile, and it always meets the maximum operating speed requirement. From Fig. 19(d), it can be observed that as wear depth increases, the lateral ride comfort of the carbody corresponding to the Opt A profile continues to outperform that of the JM_3 profile, with no signs of deterioration in stability or ride comfort.

5. Conclusion

(1) This paper uses the method of describing the wheel profile with arcs and straight lines, and uses the position parameters R_6, x_{O6}, R_7, and x_{O7} as design variables. For the CN60 and CN60N rail profiles, as well as various rail cants, wheel diameter differences, and asymmetric arrangements of the left and right rail cants, an RBFNN surrogate model is established to associate the design variables with the objective function and constraint functions. Based on the NSGA-II genetic algorithm, multi-objective optimization is performed on the JM_3 profile. K-means clustering analysis is performed on the optimization frontier to select the optimal wheel profile.

(2) Under different wheel-rail matching conditions, the nominal equivalent conicity distribution of the optimized wheel profile Opt A is more concentrated, overcoming the problem of low equivalent conicity of the original JM_3 wheel profile under high rail cant conditions, and improving the adaptability of the wheel profile to different rail profiles, rail cants, and wheel diameter differences.

(3) Establish a model of the high-speed locomotive for a certain type of power-concentrated EMU, and conduct a simulation comparison analysis of the dynamic performance of the power vehicle corresponding to the wheel profile before and after optimization. Under the four matching conditions described in this paper, the power vehicle using the optimized profile Opt A maintains essentially unchanged stability under a 1/40 rail cant condition, while achieving a significant increase in the nonlinear critical speed under a 1/20 large rail cant condition; The lateral ride index remains below 2.75 within the specified speed range, with minimal variation as speed increases. This eliminates the low-frequency swaying phenomenon caused by the original standard wheel profile failing to maintain stability under specific track conditions, and no swaying occurs during high-speed operation under all four matching conditions; Compared to the original standard profile, the curve-passing performance shows minimal differences under small-radius curve conditions. For large-radius curve conditions, curve-passing performance is significantly improved, with maximum reductions of 35.7% and 37.5% in wheelset lateral forces and derailment coefficients, respectively. At the same time, the wheel profile wear performance before and after optimization is roughly the same. With the accumulation of service mileage, the optimized profile Opt A consistently exhibits better lateral stability and ride comfort than the original JM3 profile, with no performance degradation observed.

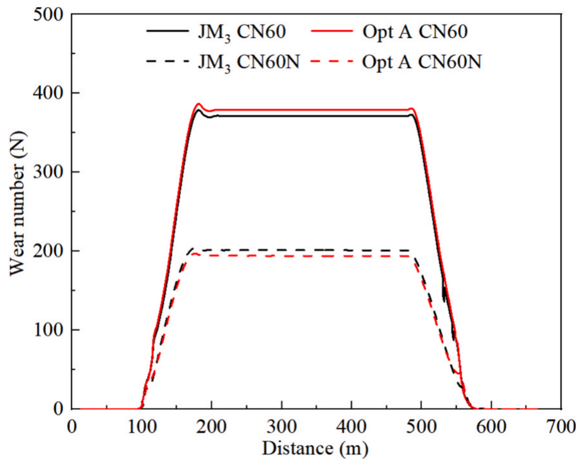

Fig. 18. Comparison of wear number.

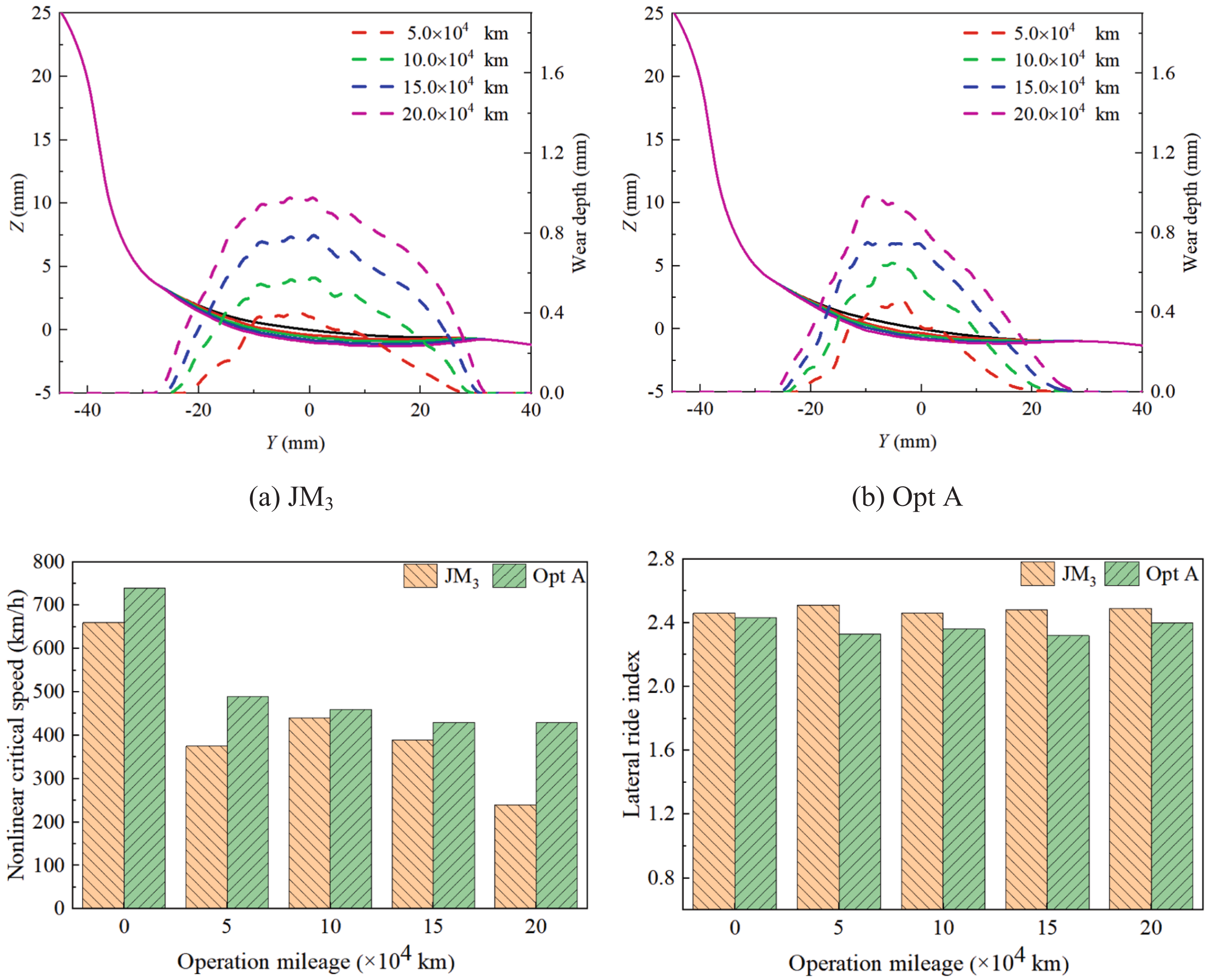

(a) JM_3 (b) Opt A

(c) Nonlinear critical speed (d) Lateral ride index of carbody

Fig. 19. Comparison of wheel profile wear and dynamic evolution.

CRediT authorship contribution statement

Fanyu Meng: Writing – original draft, Validation, Methodology, Formal analysis, Conceptualization. **Yuan Yao:** Software, Funding acquisition, Formal analysis. **Qun Ma:** Software, Methodology, Formal analysis. **Haohao Wei:** Writing – review & editing, Resources, Conceptualization.

Declaration of competing interest

The authors declare that they have no known competing financial interests or personal relationships that could have appeared to influence the work reported in this paper.

Acknowledgments

This work was supported by the National Natural Science Foundation of China [grant numbers 52372403, U2268211], and the National Railway Group Science and Technology Program [grant number N2023J071].

Data availability

The data that has been used is confidential.

References

[1] Z.Z. Shao, Research review on dynamic issue of 160 km/h Power Concentrated EMU, Railway Locomotive and Car 41 (06) (2021) 1–8.
[2] X.S. Jin, Research progress of high-speed wheel-rail relationship, Lubricants 10 (10) (2022) 248.
[3] T. Matsudaira, Hunting problem of high-speed railway vehicles with special reference to bogie design for the new Tokaido line, Proc. Inst. Mech. Eng. 180 (6) (1965) 58–66.
[4] S.G. Absel, N.K. Cooperrider, An equivalent linearization algorithm for nonlinear system limit cycle analysis, J. Dyn. Syst. Measur. Control 107 (2) (1985) 117–122.
[5] I.Y. Shevtsov, V.L. Markine, C. Esveld, Optimal design of wheel profile for railway vehicles, Wear 258 (7–8) (2005) 1022–1030.
[6] D. Cheng, C.G. Wang, J.Z. Liu, et al., Research on the mathematical model for wheel profile optimization with arc parameters as design variables, China Railway Sci. 32 (6) (2011) 107–113.
[7] Y.G. Ye, Y.Y. Qi, D.C. Shi, et al., Rotary-scaling fine-tuning (RSFT) method for optimizing railway wheel profiles and its application to a locomotive, Railway Eng. Sci. 28 (2) (2020) 160–183.
[8] G. Shen, J.B. Ayasse, H. Chollet, et al., A unique design method for wheel profiles by considering the contact angle function, Proc. Inst. Mech. Eng. Part F: J. Rail Rapid Transit 217 (1) (2003) 25–30.
[9] H. Jahed, B. Farshi, M.A. Eshraghi, et al., A numerical optimization technique for design of wheel profiles, Wear 264 (1–2) (2008) 1–10.
[10] O. Polach, Wheel profile design for target conicity and wide tread wear spreading, Wear 271 (1–2) (2011) 195–202.
[11] D.B. Cui, L. Li, X.S. Jin, et al., Optimal design of wheel profiles based on weighed wheel/rail gap, Wear 271 (1–2) (2011) 218–226.
[12] J. Santamaria, J. Herreros, E.G. Vadillo, et al., Design of an optimised wheel profile for rail vehicles operating on two-track gauges, Veh. Syst. Dyn. 51 (1) (2013) 54–73.
[13] F. Gan, H.Y. Dai, M.R. Chi, et al., A reverse optimal design method for wheel tread of railway vehicle, J. China Railway Soc. 37 (9) (2015) 17–24.
[14] D. Cheng, C. Sun, X.Y. Hu, et al., Wheel profile optimization of CRH3 EMU oriented to carbody shaking caused by low equivalent conicity, China Rail. Sci. 41 (6) (2020) 135–144.
[15] Y.Y. Qi, H.Y. Dai, F. Gan, et al., Wheel profile optimization of CRH3 type of EMU based on wheel wear and passenger comfort, J. Vibrat. Shock 40 (18) (2021) 148–155.
[16] E.N. Gao, G.Q. Tao, D.X. Ren, et al., Multi-objective optimisation of a metro wheel profile to reduce wheel flange wear and RCF considering the distribution density of wheel−rail contact points, Veh. Syst. Dyn. 63 (2) (2025) 351–374.
[17] F.T. Lin, S. Zhou, X.Q. Dong, et al., Design method of LM thin flange wheel profile based on NURBS, Veh. Syst. Dyn. 59 (1) (2021) 17–32.
[18] J.F. Sun, M.R. Chi, X.S. Jin, et al., Experimental and numerical study on carbody hunting of electric locomotive induced by low wheel-rail contact conicity, Veh. Syst. Dyn. 59 (2) (2021) 203–223.
[19] H. Li, T. Tan, S. Stichel, et al., Investigating hunting stability failure in a high-speed locomotive: a comparative analysis of evaluation methods for typical worn wheel treads, Eng. Fail. Anal. 174 (2025) 109482.
[20] H.X. Gao, J.F. Sun, X.H. Chen, et al., A novel wheel wear indicator in regard to wheel-rail contact parameters and vehicle hunting stability, Eng. Fail. Anal. 167 (2025) 108967.
[21] Y.B. Zhou, M.R. Chi, W.B. Cai, et al., Analysis of abnormal carbody lateral low-frequency vibration in intercity EMU trains caused by double-hollow worn wheel profiles, Eng. Fail. Anal. 167 (2025) 109065.
[22] Z.C. Zhang, G. Li, R.T. Du, et al., Research on transverse vibration problem for the power car of power concentrated EMU, Railway Locomotive Car 40 (3) (2020) 1–6.
[23] X. Du, G.Q. Tao, C. Yang, et al., Influence of different rail cants on dynamical characteristics of high-speed railway vehicles, J. Southwest Jiaotong Univ. 57 (2) (2022) 286–294.
[24] G. Li, R.D. Wu, X.X. Deng, et al., Suspension parameters matching of high-speed locomotive based on stability/comfort Pareto optimization, Veh. Syst. Dyn. 60 (11) (2022) 3848–3867.
[25] Y. Yao, G. Li, S.L. Liang, et al., Optimal matching method for suspension parameters of high-speed train bogie based on robust hunting stability, J. China Rail. Soc. 43 (8) (2021) 35–44.
[26] Y.H. Chen, J.X. Li, G.E. Zheng, et al., Metro wheel profile design with low flange wear based on multi-objective optimization, J. Mech. Eng. 61 (8) (2025) 261–271.
[27] F.Y. Meng, L.J. Shen, X.X. Deng, et al., Optimization of JM3 wheel profile considering the equivalent conicity dispersion, J. Southwest Jiaotong Univ. 60 (2) (2025) 346–355.
[28] TB/T 449-2016. Wheel profile for locomotive and car. National Railway Administration, China, 2016.
[29] GB/T 5599-2019. Specification for dynamic performance assessment and testing verification of rolling stock. National Railway Administration, China, 2019.
[30] J.J. Kalker, A fast algorithm for the simplified theory of rolling contact, Veh. Syst. Dyn. 11 (1) (1982) 1–13.
[31] G. Li, Y. Zhou, Y. Yao, et al., Application of yaw dampers with frequency-selective damping to improve the locomotive adaptability to low/high conicity stability, Proc. Inst. Mech. Eng., Part F: J. Rail Rapid Transit 237 (6) (2023) 784–795.
[32] Y.D. Song, T. Qin, Y. Yao, et al., Investigation on aerodynamic fluid–structure coupling vibration of 160 km/h EMU tail in single-track tunnels, Int. J. Struct. Stab. Dyn. 24 (18) (2023) 2450197.
[33] K. Elsayed, C. Lacor, Robust parameter design optimization using Kriging, RBF and RBFNN with gradient-based and evolutionary optimization techniques, Appl. Math Comput. 236 (2014) 325–344.
[34] R. Jin, W. Chen, T.W. Simpson, Comparative studies of metamodelling techniques under multiple modelling criteria, Struct. Multidiscip. Optim. 23 (1) (2001) 1–13.
[35] T.W. You, D. Gong, J.S. Zhou, et al., Frequency response function-based model updating of flexible vehicle body using experiment modal parameter, Veh. Syst. Dyn. 60 (11) (2022) 3930–3954.
[36] T.W. Anderson, An introduction to multivariate statistical analysis, 3rd ed., John Wiley & Sons, Hoboken, 2003.
[37] H.L. Shi, R. Luo, J. Zeng, Review on domestic and foreign dynamics evaluation Criteria of high speed train, J. Traffic Transport. Eng. 21 (1) (2021) 36–58.
[38] A. Bracciali, G. Megna, Contact mechanics issues of a vehicle equipped with partially independently rotating wheelsets, Wear 366–367 (2016) 233–240.
[39] F. Braghin, R. Lewis, R.S. Dwyer-Joyce, et al., A mathematical model to predict railway wheel profile evolution due to wear, Wear 261 (11–12) (2006) 1253–1264.